Supplemental Document

optica

Optical matter machines: angular momentum conversion by collective modes in optically bound nanoparticle arrays: supplement

JOHN PARKER,[1,3] CURTIS W. PETERSON,[2,3] YUVAL YIFAT,[3] STUART A. RICE,[2,3] ZIJIE YAN,[4] STEPHEN K. GRAY,[5] AND NORBERT F. SCHERER[2,3,*]

[1]*Department of Physics, The University of Chicago, Chicago, Illinois 60637, USA*
[2]*Department of Chemistry, The University of Chicago, Chicago, Illinois 60637, USA*
[3]*James Franck Institute, The University of Chicago, Chicago, Illinois 60637, USA*
[4]*Department of Applied Physical Sciences, University of North Carolina at Chapel Hill, Chapel Hill, North Carolina 27599, USA*
[5]*Center for Nanoscale Materials, Argonne National Laboratory, Lemont, Illinois 60439, USA*
[*]*Corresponding author: nfschere@uchicago.edu*

Supplement DOI: https://doi.org/10.6084/m9.figshare.12794690

Parent Article DOI: https://doi.org/10.1364/OPTICA.396147

Supplementary Information – Optical matter machines: angular momentum conversion by collective modes in optically bound nanoparticle arrays

JOHN PARKER,[1,3] CURTIS W. PETERSON,[2,3] YUVAL YIFAT, [3] STUART A. RICE,[2,3] ZIJIE YAN,[4] STEPHEN K. GRAY,[5] AND NORBERT F. SCHERER[2,3,*]

[1]Department of Physics, The University of Chicago, Chicago, IL 60637, USA
[2]Department of Chemistry, The University of Chicago, Chicago, IL 60637, USA
[3]James Franck Institute, The University of Chicago, Chicago, IL 60637, USA
[4]Department of Applied Physical Sciences, University of North Carolina at Chapel Hill, Chapel Hill, NC 27599, USA
[5]Center for Nanoscale Materials, Argonne National Laboratory, Lemont, IL 60439, USA
[*]nfschere@uchicago.edu

A. Generalized Multiparticle Mie Theory (GMMT) simulations

GMMT is a very fast and accurate method for solving the electrodynamics of a collection of particles making up a cluster. GMMT works on the principle of generalizing the single particle Mie theory to include arbitrary source illumination and matching the boundary conditions on multiple particle surfaces. We summarize here the important parts of GMMT; the complete theory is described in detail elsewhere. [1] All electrodynamic simulations were performed using our open sourced code MiePy, available online. [2]

Field expansions in GMMT. The incident and scattered fields around particle j are expanded into the vector spherical harmonic wave (VSHW) functions.

$$\boldsymbol{E}^{j}_{\text{inc}}(\boldsymbol{r}) = -\sum_{n=1}^{N_{\max}}\sum_{m=-n}^{n} iE_{mn}\left[p^{j}_{mn}\boldsymbol{N}^{(1)}_{mn}(\boldsymbol{r}) + q^{j}_{mn}\boldsymbol{M}^{(1)}_{mn}(\boldsymbol{r})\right] \tag{S1}$$

$$\boldsymbol{E}^{j}_{\text{scat}}(\boldsymbol{r}) = \sum_{n=1}^{N_{\max}}\sum_{m=-n}^{n} iE_{mn}\left[a^{j}_{mn}\boldsymbol{N}^{(3)}_{mn}(\boldsymbol{r}) + b^{j}_{mn}\boldsymbol{M}^{(3)}_{mn}(\boldsymbol{r})\right] \tag{S2}$$

The functions $\boldsymbol{N}_{mn}$ and $\boldsymbol{M}_{mn}$ are the electric and magnetic modes, respectively, of order n and azimuthal index m. The total scattered field at a position $\boldsymbol{r}$ is computed as a sum over individual particle expansions

$$\boldsymbol{E}_{\text{scat}}(\boldsymbol{r}) = \sum_{j}\boldsymbol{E}^{j}_{\text{scat}}(\boldsymbol{r}-\boldsymbol{r}_j) \tag{S3}$$

For a cluster of particles, the total scattered field can be expanded around a single origin, effectively treating the cluster as a single scattering object

$$\boldsymbol{E}_{\text{scat}}(\boldsymbol{r}) = \sum_{n=1}^{N_{\max}}\sum_{m=-n}^{n} iE_{mn}\left[a_{mn}\boldsymbol{N}^{(3)}_{mn}(\boldsymbol{r}) + b_{mn}\boldsymbol{M}^{(3)}_{mn}(\boldsymbol{r})\right] \tag{S4}$$

where the cluster expansion coefficients, a_{mn} and b_{mn}, are obtained by translating the particle expansion coefficients to the origin using the VSHW function translational addition theorem [3]

$$a_{mn} = \sum_{j}\sum_{v=1}^{N_{\max}}\sum_{u=-v}^{v} A^{(1)0j}_{mnuv}a^{j}_{uv} + B^{(1)0j}_{mnuv}b^{j}_{uv} \tag{S5}$$

$$b_{mn} = \sum_{j}\sum_{v=1}^{N_{\max}}\sum_{u=-v}^{v} B^{(1)0j}_{mnuv}a^{j}_{uv} + A^{(1)0j}_{mnuv}b^{j}_{uv} \tag{S6}$$

Multipole decomposition of the scattering and absorption cross-sections. With the cluster expansion coefficients determined, the scattering, extinction, and absorption cross-sections of the entire cluster are given by

$$C_{\text{scat}} = \frac{4\pi}{k^2} \sum_{n=1}^{N_{\max}} \sum_{m=-n}^{n} |a_{mn}|^2 + |b_{mn}|^2 \tag{S7a}$$

$$C_{\text{ext}} = \frac{4\pi}{k^2} \sum_{n=1}^{N_{\max}} \sum_{m=-n}^{n} \text{Re}\left\{a_{mn} p_{mn}^* + b_{mn} q_{mn}^*\right\} \tag{S7b}$$

$$C_{\text{abs}} = C_{\text{ext}} - C_{\text{scat}} \tag{S7c}$$

Each term in the summation provides the contribution of the given mode to the total cross-section. These equations are used for the scattered field analysis of the OM gear in Fig. 2(a,b).

Multipole decomposition of the optical angular momentum. The total rate of angular momentum scattered by the cluster can be obtained by analytically integrating the Maxwell stress tensor around a closed surface containing all of the particles. [4] The expression for the z-component of the rate of outgoing angular momentum, $\dot{L}_z$, is

$$\dot{L}_z = \frac{2\pi}{k^3} \sum_{n=1}^{N_{\max}} \sum_{m=-n}^{n} m\left\{\varepsilon_b |a_{mn}|^2 + \mu_b |b_{mn}|^2 - \text{Re}\left[\varepsilon_b a_{mn} p_{mn}^* + \mu_b b_{mn} q_{mn}^*\right]\right\} \tag{S8}$$

where ε_b and μ_b are the background permittivity and permeability, respectively. This can be related to the scattering and absorption cross-sections on a term-by-term basis. For a RHC polarized plane wave, $p_{mn} = q_{mn} = 0$ if $m \neq 1$. So if $m \neq 1$:

$$\dot{L}_z^{mn1} = \frac{m\varepsilon_b}{2k} C_{\text{scat}}^{mn1} \tag{S9}$$

$$\dot{L}_z^{mn2} = \frac{m\mu_b}{2k} C_{\text{scat}}^{mn2} \tag{S10}$$

and if $m = 1$:

$$\dot{L}_z^{1n1} = -\frac{\varepsilon_b}{2k} C_{\text{abs}}^{1n1} \tag{S11}$$

$$\dot{L}_z^{1n2} = -\frac{\mu_b}{2k} C_{\text{abs}}^{1n2} \tag{S12}$$

The total rate of outgoing angular momentum is then a sum over all terms

$$\dot{L}_z = \sum_{r=1}^{2} \sum_{n=1}^{N_{\max}} \sum_{m=-n}^{n} \dot{L}_z^{mnr} \tag{S13}$$

The net torque on the cluster in response to the outgoing angular momentum contains both spin (internal) and orbital (external) components

$$\tau_z^{\text{net}} = \hat{\boldsymbol{z}} \cdot \sum_i \boldsymbol{r}_i \times \boldsymbol{F}_i + \boldsymbol{\tau}_i = -\dot{L}_z \tag{S14}$$

These equations are similar to those reported by others. [5]

B. Coupling GMMT simulations with Brownian Dynamics (BD) simulations

The electrodynamic force acting on each particle can be determined by integrating the MST around a closed surface, similar to the optical torque. This can be carried out analytically as a sum over particle expansion coefficients. [4] These forces can then be used in a Brownian dynamics time-stepping algorithm to simulate the driven and random motion of the particle system. Brownian dynamics is equivalent to the overdamped Langevin equation

$$\frac{d\boldsymbol{r}_i}{dt} = \frac{1}{\gamma_i}\boldsymbol{F}_i + \sqrt{\frac{2k_BT}{\gamma_i}}\boldsymbol{\eta}_i(t) \tag{S15}$$

where $\boldsymbol{r}_i$ is the position of particle i, $\gamma_i = 6\pi\mu R_i$ is the friction coefficient of particle i with radius R_i, $T = 300\,\mathrm{K}$ is the temperature of the medium, and $\boldsymbol{\eta}_i(t)$ is a delta-correlated random normal vector with mean 0 and variance 1. The force on each particle, $\boldsymbol{F}_i$, is due to electrodynamic forces (calculated by GMMT) and screened Coulomb interactions. The screened Coulomb interaction is a pairwise repulsive force given by

$$\boldsymbol{F}_{ij}^{\text{Coulomb}} = A(R_i + R_j)\hat{\boldsymbol{r}}_{ij} \exp\left[-(r_{ij} - (R_i + R_j))/\lambda_D\right] \tag{S16}$$

where $\lambda_D = 27\,\mathrm{nm}$ is the Debye length of the solution (used in the experiment), r_{ij} is the center-to-center interparticle separation, and A is a constant. [6, 7]

C. Optical setup: simulation and experiment comparison

The experimental optical setup has a $\lambda = 800\,\mathrm{nm}$ laser beam incident on a spatial light modulator (SLM; Meadowlark). The SLM has a parabolic phase profile ($\varphi = \alpha\rho^2$), causing the beam to ultimately be defocused at the sample with an inward directed phase gradient. [8] A long focal length lens (f1) placed after the SLM is used to reshape the beam diameter and underfill the back aperture (BA). The beam is slightly diverging at the objective lens and is converging at the plane of the sample. The optical setup for simulations mimics the experiment one without the need of the first lens (f1) since the beam diameter can be resized at will.

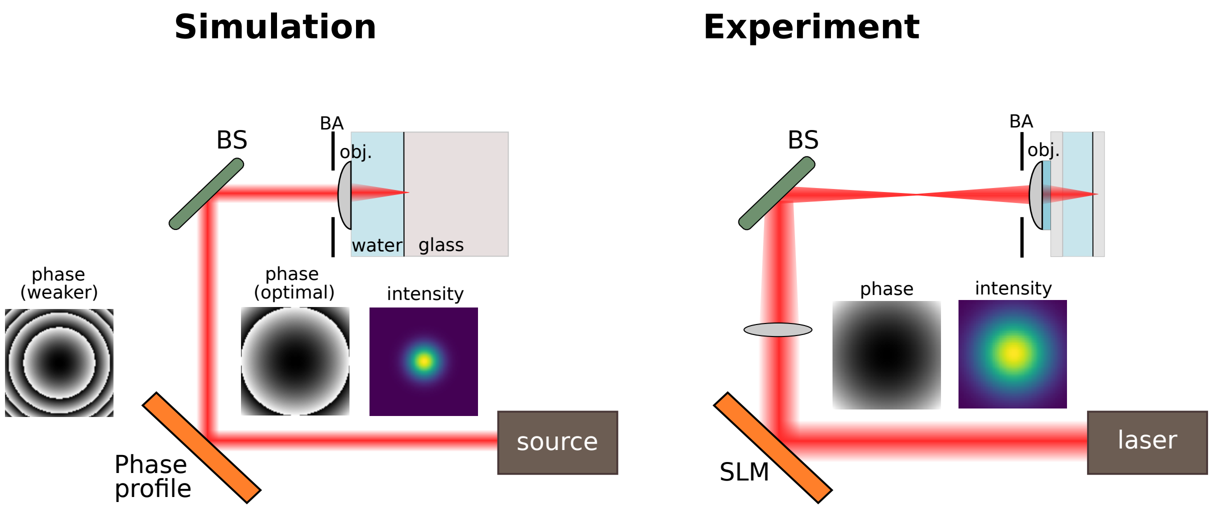

Fig. S1. Effective optical setups for simulation (left) and experiment (right). In the electrodynamics simulations, a parabolic phase profile is used to model the SLM in experiment. In experiment, the back aperture is underfilled using along a long focal length lens; this is done in simulation by adjusting the width at the source. Note that not all optics are shown for the experiment.

D. Collective scattering resonance of OM arrays converges to the lattice plasmon resonance

As more particles are added to a hexagonally ordered optical matter array, the collective scattering resonance (CSR) becomes spectrally more narrow and approaches the lattice plasmon resonance (LPR). [9] Fig. S2 shows the results of simulations of 1-19 particles and compares their scattering spectra to that of 331 particles to demonstrate this convergence.

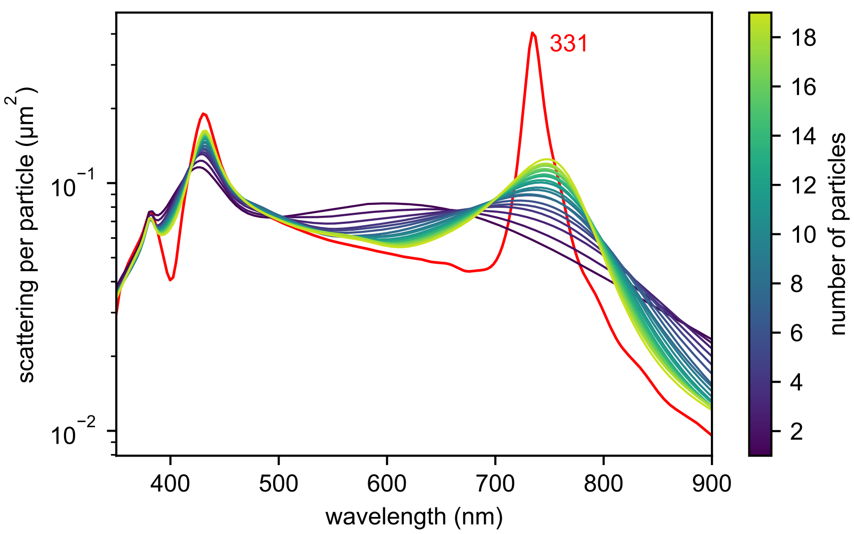

Fig. S2. Scattering spectra of optical matter arrays built on a hexagonal lattice. A CSR appears near 750 nm in the OM arrays consisting of 2-19 particles. In the limit of a larger lattice (red curve; 331 particles, or 10 filled subshells), the CSR approaches a narrower resonance as is expected of a LPR.

E. Additional modes scattered by the OM gear

Fig. 2(d-f) in the main text shows the angular distribution of the 3 collective scattering modes of the OM gear that carry the largest quantities of angular momentum. There are many more modes that arise and contribute to the scattering cross-section of the CSR; all of the electric modes are shown in Fig. S3. The allowed collective scattering modes obey the angular selection rule of Eq. (2) in the main text. Modes are ordered from largest (a) to smallest (k) quantity of angular momentum at the 800 nm incident wavelength. Modes such as $e_{1,1}$ and $e_{5,1}$ are responsible for the strong forward and backward lobes in the total scattering of the OM gear, shown in Fig. 2(c).

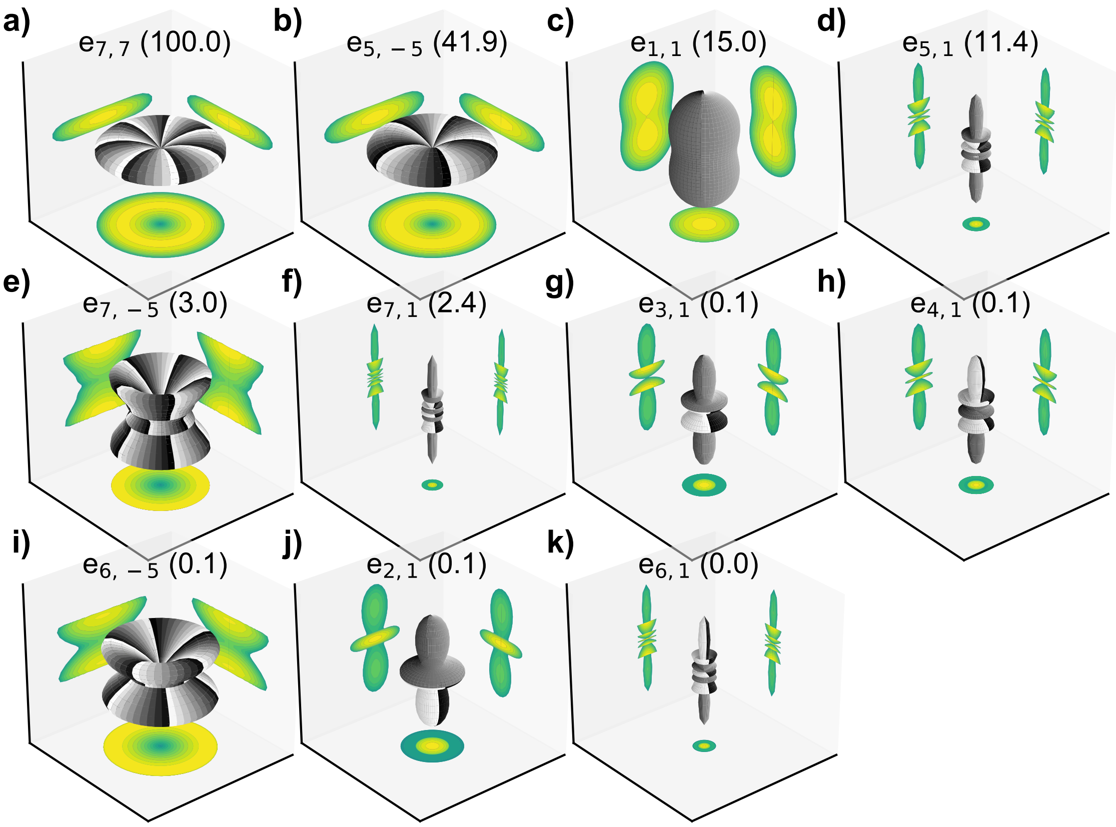

Fig. S3. Far-field scattering patterns for all of the relevant electric modes scattered by the 7NP OM gear (up to $n = 7$). They are ordered from largest quantity of angular momentum (a) to least quantity of angular momentum (k). The value in parentheses is a normalized measure of the mode's angular momentum.

F. Analysis of the probe particle

Trapping with an inward phase gradient. Assembly of the OM machine involves adding a probe particle to the OM gear – the analog of the small gear in the planetary gear machine. Confinement of the probe particle can be achieved using a combination of intensity and phase gradient optical forces. The focal plane of the incident Gaussian beam can be defocused beyond the plane of the sample to obtain a parabolic phase profile with an inward phase gradient. This leads to phase gradient forces that can increase the stability of NP assemblies relative to using just intensity gradient forces [8]. The phase of a Gaussian beam focused at $z = 0$ a distance ρ from the beam's axis is

$$\varphi(\rho, z) = \frac{k\rho^2}{2R(z)} \tag{S17}$$

where $k = 2\pi n/\lambda$ is the wavenumber and $R(z)$ is the beam's radius of curvature

$$R(z) = z\left[1 + (z_R/z)^2\right] \tag{S18}$$

and $z_R = \pi w_0^2/\lambda$ is defined as the Rayleigh range and w_0 is the beam's waist radius. The radius of curvature is minimized when $z = \pm z_R$, which results in the largest possible phase gradient. We take $z = +z_R$ to obtain a maximum inward phase gradient force in the simulations. An analogous situation is created empirically in the experiments.

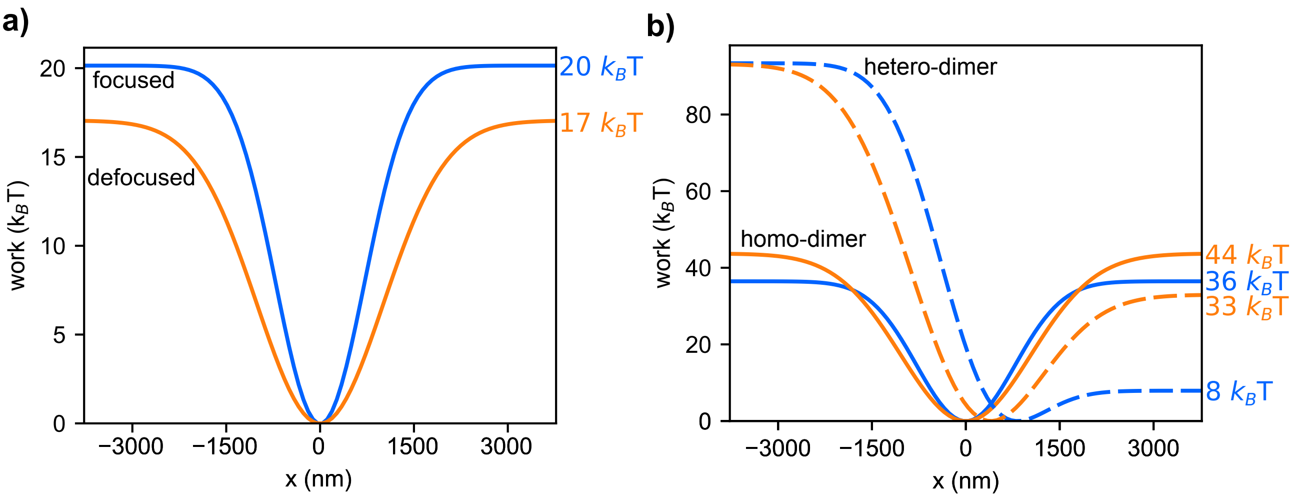

Fig. S4. Comparison of the trapping potentials of monomers, homo-dimers, and hetero-dimers using a focused beam vs. an optimally defocused (converging towards $z = z_R$) beam with an inward phase gradient. The x-axis values represent the transverse position of the dimer's center-of-mass in the optical trap. (a) Trapping potential of a single nanoparticle for focused (blue) and optimally defocused (orange) beams. (b) Trapping potentials of a homo-dimer (solid) and hetero-dimer (dashed) for focused and optimally defocused beams. The work is expressed in units of thermal energy, $k_B T$, for $T = 298\,\text{K}$.

Trapping potentials for a single NP, Fig. S4(a), show that a focused beam has a larger trapping stiffness than the optimally defocused beam ($z = z_R$). That is, the intensity gradient of light provides better confinement than the phase gradient of light for a single NP. However, Fig. S4(b) shows that the situation is reversed for the trapping potentials of a rigid dimer. For a homo-dimer (diameter 150 nm), the defocused beam has a broader but deeper trapping potential. For a hetero-dimer (diameters 150 nm and 200 nm), there are known non-reciprocal forces that cause the small particle to 'chase' the bigger particle [10]. This phenomena makes the hetero-dimer difficult to trap, but the defocused beam provides a way to increase the trapping stiffness of these asymmetrical structures.

The OM gear–probe machine is also asymmetrical in shape and will experience these non-reciprocal forces. The inward phase gradient turns out to be *essential* to assembling and trapping these machines and enabling their counter-rotation through electrodynamic driven forces and thermal fluctuations. An example trajectory of the OM machine with a focused Gaussian beam is shown in Fig. S5. The probe particle quickly escapes from the trap. The OM gear, initially 'pulled' away from the center of the trap by the probe, is restored to the center of the trap as the probe particle diffuses away.

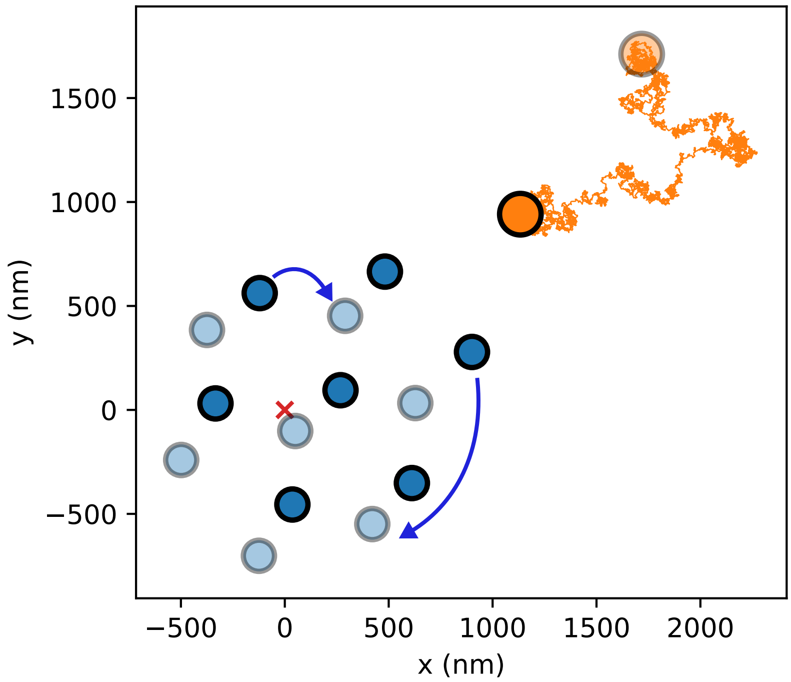

Fig. S5. Trajectories of the NPs in the OM machine assembled with a focused ($z = 0$) Gaussian beam in a Brownian dynamics simulation. Without an inward phase gradient from a defocused and converging beam, the probe particle escapes the trap. The red x indicates the center of the optical trap.

Influence of the probe on the OM gear. Ideally, the probe particle has minimal impact on the OM gear structure it probes. Generally, probe particles with a smaller radius will scatter less and therefor have less of an influence on the OM gear's structure. To study this influence, the interparticle separations of the NPs in the OM gear are calculated in the presence of a probe particle at different radii. This is done by performing a deterministic dynamics ($T = 0$ Brownian dynamics) simulation and extracting the steady state interparticle separations. Fig. S6 shows an increase in interparticle spacing as the probe particle radius is increased. The blue curve corresponds to the pair of particles in the OM gear closest to the probe particle; they are deformed to be closer to each other. The interparticle separations that are increasing with probe size are particle pairs furthest from the probe particle. This shift in interparticle spacing can, in principle, cause the sign of the torque on the OM gear to switch from negative to positive.

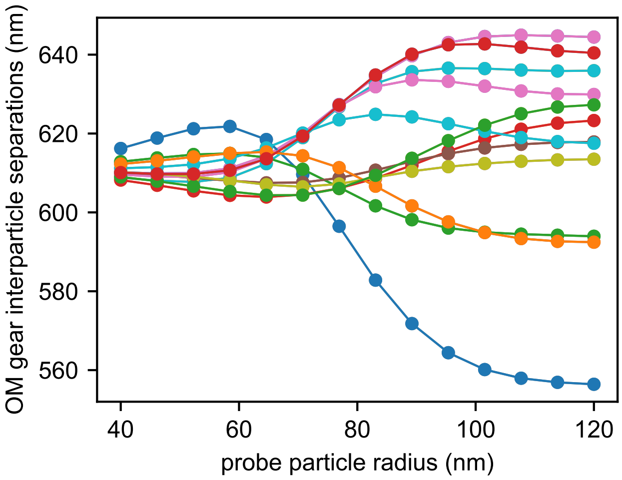

Fig. S6. An increase in the probe particle's radius results in larger deformation of the OM gear. The probe particle electrodynamically interacts with the 7NP OM gear, resulting in a shift in the interparticle separations of the OM gear. Each color corresponds to a given pair of NPs in the OM gear.

Effects of a smaller probe particle. The results in Fig. S6 suggest that a probe particle smaller than the other (R = 75 nm) NPs in the OM gear is preferred since it deforms the gear less than a larger probe. However, Brownian dynamic simulations (T = 298) with a smaller probe (R = 60 nm) particle reveal an undesirable effect: the smaller probe inserts itself into the gear and expels one of the other particles to be outside the OM gear. This insertion and expulsion behavior is demonstrated in Fig. S7. Generally, a smaller NP will "chase" a larger NP, so that a smaller probe particle will always be pushing its way inward until it breaks into the gear. On the other hand, a larger probe particle will be chased by the smaller gear particles, keeping the probe on the periphery of the gear.

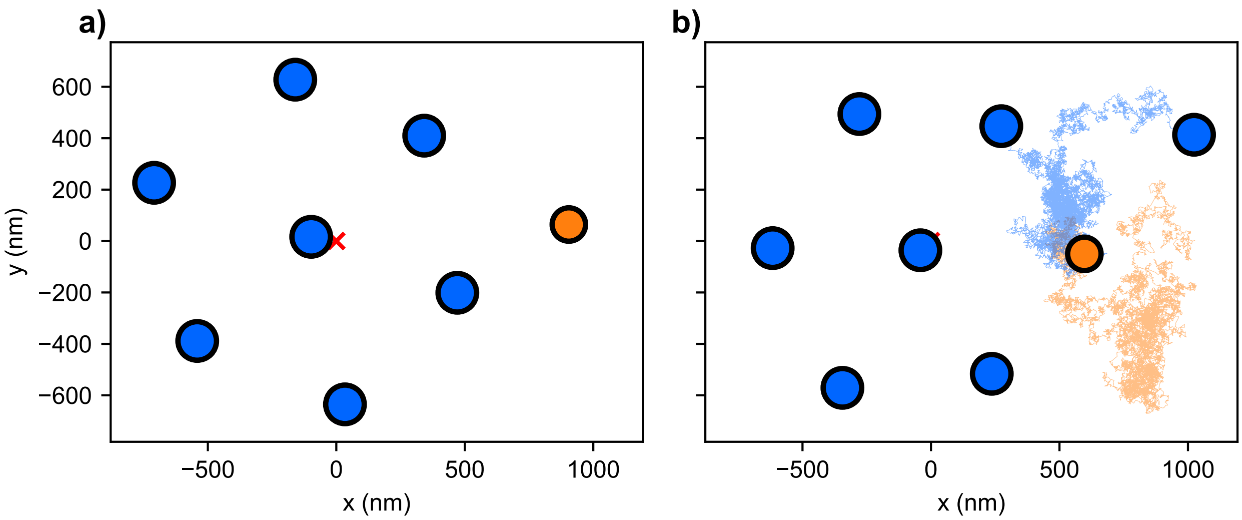

Fig. S7. A smaller probe particle will insert itself into the OM gear and expel a NP to be outside the OM gear. (a) Starting a Brownian dynamics (T = 298 K) with the smaller probe particle (orange) outside of the OM gear. (b) After some time, the probe particle exchanges positions with one of the nanoparticles in the OM gear (blue).

Parameter space search. A parameter sweep over reasonable values was performed to determine the optimal simulation parameters to obtain a stable, trapped OM machine with counter-rotation. The incident beam power (P) was varied from 10 mW to 50 mW; the probe particle diameter (D) from 180 nm to 220 nm; the beam waist (w_0) from 1200 nm to 2500 nm; the beam defocus (z) from $z_R/2$ to z_R, where z_R is the Rayleigh range. Of 108 simulations with different parameters, about 10 were stable and showed substantial clockwise thermal hopping of the probe particle. The other simulations either had too much thermal noise such that the probe escaped while the gear rearranged, or were too stiff such that the machine was stable but the probe particle could not hop. The best demonstration of counter-rotation was obtained for the values: P = 40 mW, w_0 = 2500 nm, D = 200 nm, and $z = z_R/1.2$.

G. Hydrodynamic coupling effects in the OM machine

Stokesian dynamics is an extension of Langevin dynamics that incorporates the hydrodynamic coupling interactions due to fluid flow in the medium. [11] In particular, rotation-translation (RT) coupling has been shown to be an important consideration. [12] In the OM machine, the Ag nanoparticles are spinning with a positive torque due to the incident spin of the RHC polarized light. This spinning leads to vorticity in the surrounding fluid that can generate additional translational motion, see Fig. S8(a).

Fig. S8(b) shows the angles of the OM gear and probe, averaged over an ensemble of 20 trajectories. The hydrodynamic coupling causes the OM gear to rotate with a positive angular velocity, as opposed to the negative angular velocity without hydrodynamic coupling in Fig. 4(d). However, we still obtain the clockwise biased hopping of the probe particle. Note that the hydrodynamic interactions implemented here do not take into account the water–glass interface, which might have a significant effect. [13]

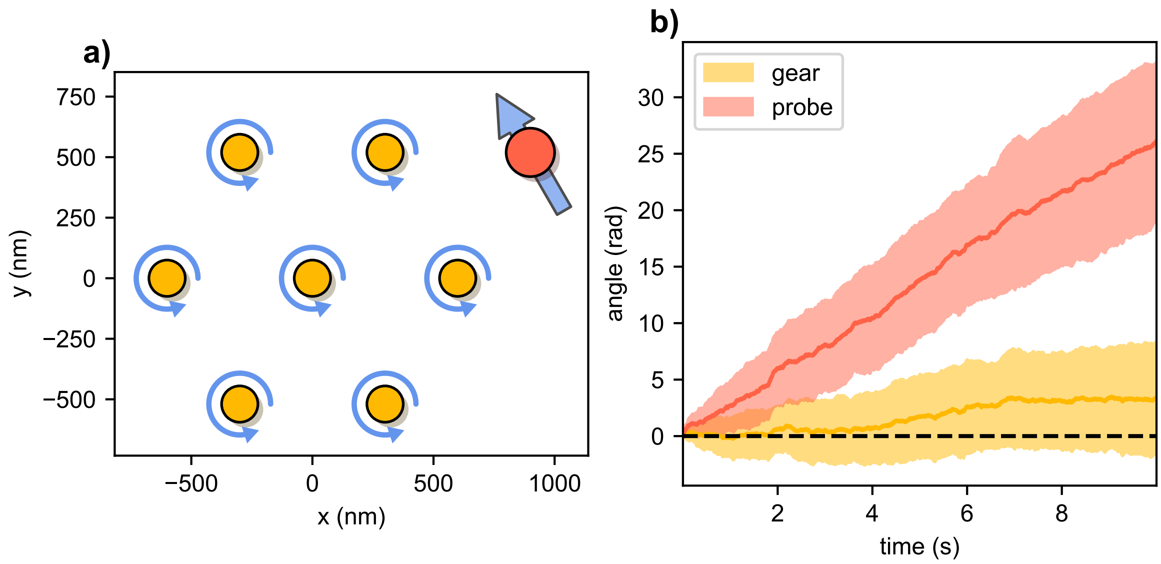

Fig. S8. Hydrodynamic interactions in the OM gear – probe particle system. **(a)** The spinning of the particles inside the OM gear leads to translational fluid flow at the probe particle (hydrodynamic RT coupling). **(b)** Ensemble results (over 20 trajectories) for the angles of the OM gear and probe over time.

H. Experimental results of the 7NP OM gear

Fig. S9 demonstrates experimentally the counter-rotation for a 7NP OM gear–probe machine. While the counter-rotation was observed in this case, the effect was less ubiquitous than the 8NP OM gear demonstrated in Fig. 4.

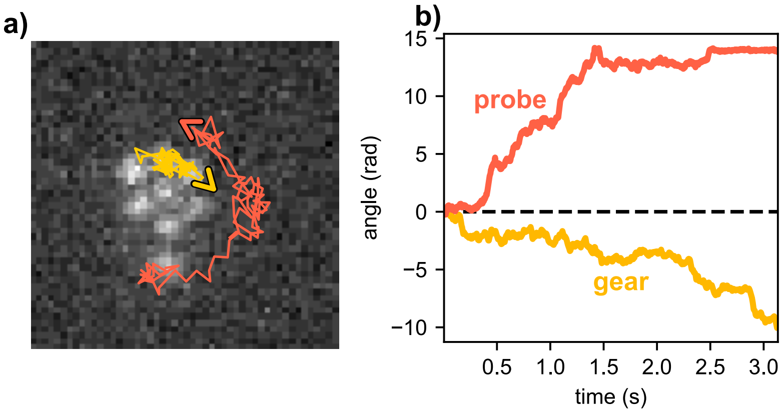

Fig. S9. Experimental observation of the counter-rotational dynamics of the 7NP OM gear–probe machine. (left) Still-image and superimposed trajectories of the gear (yellow for NP) and probe (orange). (right) Angular trajectory of the OM gear and probe over time.

I. Analysis of the e_7 mode with the probe and with thermal fluctuations

While the gear has a perfect 6-fold symmetry, the gear + probe system does not. If the probe were a small perturbation, this would not significantly change the angular momentum scattered by the array. However, since the probe is larger particle its causes a large perturbation. Fig. S10 shows the effect the probe has on the amount of angular momentum scattered into the $e_{7,7}$ mode, an amount that is not insignificant.

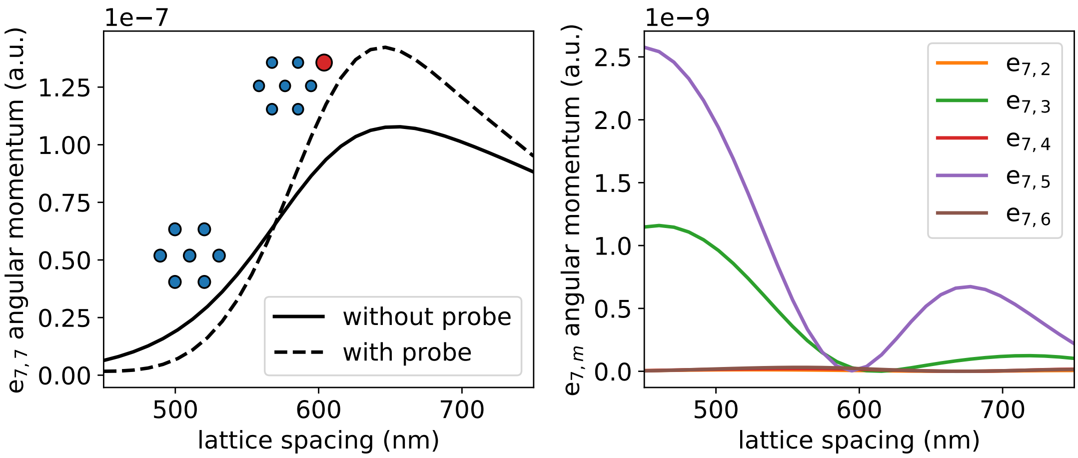

Fig. S10. Effect of the probe on the e_7 mode of the gear. (left) The angular momentum carried by the $e_{7,7}$ mode of the entire array with and without the presence of the probe particle. (right) The angular momentum carried by the $e_{7,m}$ modes of the machine with the probe where m does not satisfy the angular momentum selection rule ($m \neq$ -5,1,7). The machine without the probe does not carry any angular momentum in these modes.

Additionally, there are new angular momentum channels the array can scatter into since it is no longer 6-gold symmetric. The angular momentum carried in the $e_{7,m}$ modes for the gear–probe system is shown in Fig. S10. For the gear-only system, these modes would be prohibited and hence carry no angular momentum. The $m = 5$ and $m = 3$ contributions are largest, but still only carry about $50\times$ less than the amount in the $e_{7,7}$ mode.

Fluctuations of the particles in the gear also have an effect on the quantity of angular momentum it scatters and therefore the overall efficiency of the machine. Fig. S11 shows the fluctuations of the angular momentum in the $e_{7,7}$ mode over a short period of simulation time for the gear. The maximum possible angular momentum is scattered when the gear has perfect hexagonal (6-fold) symmetry. The average amount of angular momentum scattered while fluctuating is about 85% of its optimal value.

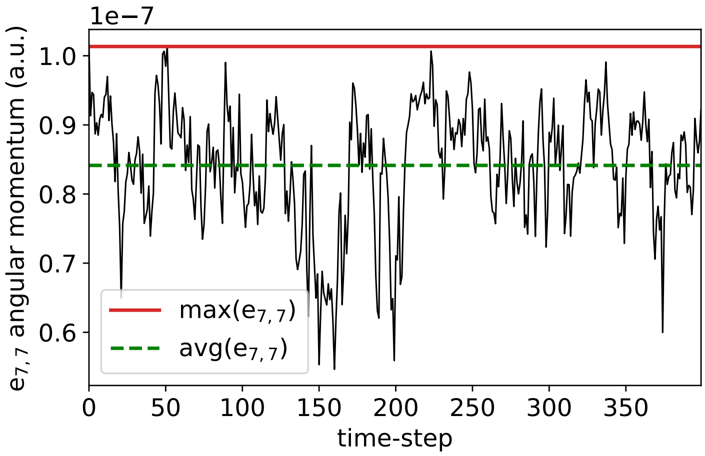

Fig. S11. Fluctuations of the angular momentum in the $e_{7,7}$ mode of the 7 particle gear array. The maximum possible quantity of angular momentum corresponds to the perfect hexagonal lattice. Brownian forces and displacements causes it to be less than this maximum value.

J. High-index dielectric OM machine

It is possible to build an OM machine out of dielectric particles instead of plasmonic particles. High-index dielectric such as silicon (Si) are good candidates due to their enhanced scattering and sharp resonances. At $\lambda = 800\,\mathrm{nm}$, silicon can be approximated with a constant index of refraction $n = 3.7$. Fig. S12(a) shows the construction of the Si machine, where the gear particles are now larger than the probe particle. Unlike the plasmonic machine, this machine is stable and does not suffer the same intrusive dynamics as shown in Fig. S7. This unique behavior is likely due to the presence of a significant magnetic dipole mode for Si nanoparticles, see Fig. S12(b).

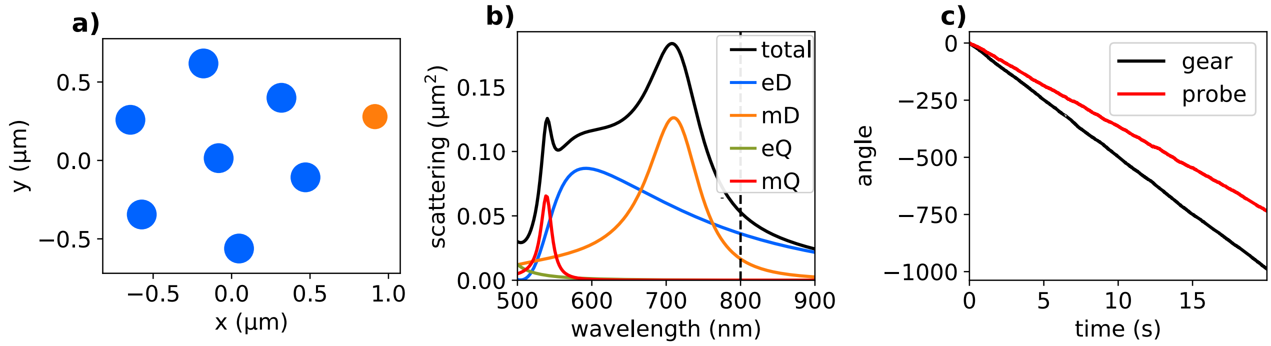

Fig. S12. Realization of a silicon optical matter machine in simulation. (a) Snapshot of the machine with a gear made of 90 nm radius Si particles and an Si probe of radius 75 nm. (b) Multipolar scattering of the 90 nm radius Si particle. (c) Angles of the gear and probe over a simulation.

Angles of the gear and probe in the Si machine are shown in Fig. S12(c). Similar to the plasmonic machine, the probe particle only hops in the counter-clockwise direction. Unlike the plasmonic machine, the gear spins much faster and with a negative torque such that counter-rotation of the gear–probe machine is not observed.

K. Efficiency of the stochastic optical matter machine

Due to the stochastic nature of the OM machine, the machine does not operate at very low or very high laser power density. If the power density of the trapping laser is too low, thermal fluctuations dominate the particle trajectories as shown in Fig. S13(a). If the power density is moderate, the electrodynamic forces become significant relative to thermal fluctuations, allowing the machine to counter-rotate as shown in Fig. S13(b). If the power density is too high, counter-rotation is not possible since the thermal fluctuations are needed for the machine to operate and the arrays rotates as a rigid lattice as shown in Fig. S13(c).

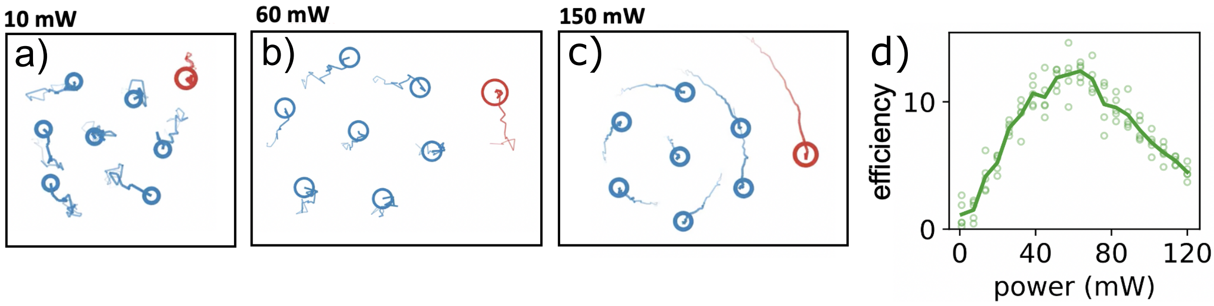

Fig. S13. Demonstrating the stochastic nature of the optical matter machine. (a) OM machine at a low laser power is dominated by thermal fluctuations. (b) OM machine at a moderate laser power is operable and exhibits counter-rotation. (c) OM machine at a high laser power is driven with one handedness and does not counter-rotate. (d) Efficiency of the Si dielectric machine as a function of the incident power. Each circle is a simulation result, with 5 simulations performed per power; the solid line is an average fit.

The efficiency of the OM machine can be defined as the rate of thermal hopping of the probe around the OM gear

$$\mathcal{E} = \lim_{t\to\infty}\left(\frac{\phi_2(t) - \phi_1(t)}{t}\right) \tag{S19}$$

In general, $\mathcal{E}$ depends on the power of the incident beam. Fig. S13(d) shows $\mathcal{E}(P)$ of the Si dielectric machine introduced in the previous section. As the power goes to zero, $\mathcal{E}(P)$ goes to zero since the machine is not operable if the gear is not a stable unit. On the other hand, as the power gets larger $\mathcal{E}(P)$ goes to zero since some thermal energy is required for the probe to hop and be driven. Consequently, the machine's efficiency is a maximum at some finite power. This type of power dependence is expected of stochastic machines.

References

1. Y.-l. Xu, “Electromagnetic scattering by an aggregate of spheres,” Appl. Opt. **34**, 4573–4588 (1995).
2. “Scherer lab,” Https://schererlab.uchicago.edu/research/theory-and-simulation.
3. S. Stein, “Addition theorems for spherical wave functions,” Q. Appl. Math. **19**, 15–24 (1961).
4. J. P. Barton, D. R. Alexander, and S. A. Schaub, “Theoretical determination of net radiation force and torque for a spherical particle illuminated by a focused laser beam,” J. Appl. Phys. **66**, 4594–4602 (1989).
5. J. Chen, J. Ng, K. Ding, K. H. Fung, Z. Lin, and C. T. Chan, “Negative Optical Torque,” Sci. Reports **4** (2015).
6. D. A. Walker, B. Kowalczyk, M. O. de la Cruz, and B. A. Grzybowski, “Electrostatics at the nanoscale,” Nanoscale **3**, 1316–1344 (2011).
7. F. Nan, F. Han, N. F. Scherer, and Z. Yan, “Dissipative Self-Assembly of Anisotropic Nanoparticle Chains with Combined Electrodynamic and Electrostatic Interactions,” Adv. Mater. **30**, 1803238 (2018).
8. Z. Yan, M. Sajjan, and N. F. Scherer, “Fabrication of a material assembly of silver nanoparticles using the phase gradients of optical tweezers,” Phys. Rev. Lett. **114**, 143901 (2015).
9. S. Zou, N. Janel, and G. C. Schatz, “Silver nanoparticle array structures that produce remarkably narrow plasmon lineshapes,” The J. Chem. Phys. **120**, 10871–10875 (2004).
10. Y. Yifat, D. Coursault, C. W. Peterson, J. Parker, Y. Bao, S. K. Gray, S. A. Rice, and N. F. Scherer, “Reactive optical matter: light-induced motility in electrodynamically asymmetric nanoscale scatterers,” Light. Sci. & Appl. **7**, 105 (2018).
11. J. F. Brady and G. Bossis, “Stokesian Dynamics,” Ann. Rev. Fluid Mech. pp. 111–157 (1988).
12. E. Dickinson, S. A. Allison, and J. A. Mccammon, “Brownian Dynamics with Rotation-Translation Coupling,” J. Chem. SOC. Faraday Trans **2**, 591–601 (1985).
13. J. W. Swan and J. F. Brady, “Simulation of hydrodynamically interacting particles near a no-slip boundary,” Phys. Fluids **19**, 113306 (2007).